Elevated Tropospheric Iodine over the Central Continental United States: Is Iodine a Major Oxidant of Atmospheric Mercury?

C. F. Lee[1,2], T. Elgiar[3], L. M. David[3,+], T. Y. Wilmot[4], M. Reza[1,2], N. Hirshorn[4,%], I. B. McCubbin[4], V. Shah[5,#], J. C. Lin[4], S. N. Lyman[3,6], A. G. Hallar[4], L. E. Gratz[7,*], and R. Volkamer[1,2]

[1]Department of Chemistry, University of Colorado Boulder, Boulder, CO, USA

[2]Cooperative Institute for Research in Environmental Sciences, Boulder, CO, USA

[3]Bingham Research Center, Utah State University, Vernal, UT, USA

[4]Department of Atmospheric Sciences, University of Utah, Salt Lake City, UT, USA

[5]School of Engineering and Applied Sciences, Harvard University, Cambridge, MA, USA

[6]Department of Chemistry & Biochemistry, Utah State University, Logan, UT, USA

[7]Environmental Studies Program, Colorado College, Colorado Springs, CO, USA

Corresponding author: Rainer Volkamer (rainer.volkamer@colorado.edu)

[+]Current affiliation: Ramboll, Fort Collins, CO, USA

[%]Current affiliation: Ramboll, New York, NY, USA

[#]Current affiliation: Science Systems and Applications, Inc., Lanham, MD, USA

*Current affiliation: Department of Chemistry and Environmental Studies Program, Reed College, Portland, OR, USA

Key Points:

- Measurements of iodine monoxide radicals at Storm Peak Laboratory are up to three times higher than predicted by GEOS-Chem.
- IO tropospheric column variability is significant and highlights a need to better understand sources and sinks of free tropospheric iodine.
- Iodine rivals bromine as an oxidant of mercury in the upper troposphere; iodine-mercury chemistry is understudied and missing in atmospheric models.

Abstract

Previous efforts to measure atmospheric iodine have focused on marine and coastal regions. We report the first ground-based tropospheric iodine monoxide (IO) radical observations over the central continental United States. Throughout April 2022, IO columns above Storm Peak Laboratory, Colorado (3220 m.a.s.l.) ranged from 0.7±0.5 to 3.6±0.5×10^{12} (average: 1.9×10^{12} molec cm^{-2}). IO was consistently elevated in air masses transported from over the Pacific Ocean. The observed IO columns were up to three times higher and the range was larger than predicted by a global model, which warrants further investigation into iodine sources, sinks, ozone loss, and particle formation. IO mixing ratios increased with altitude. At the observed levels, iodine may be competitive with bromine as an oxidant of elemental mercury at cold temperatures typical of the free troposphere (4–12km; <260K). Iodine-induced mercury oxidation is missing in atmospheric models, understudied, and helps explain model underestimation of oxidized mercury measurements.

Plain Language Summary

Halogens such as chlorine, bromine, and iodine are highly reactive gases that participate in atmospheric chemistry, including ozone destruction, particle formation, modification of greenhouse gas lifetime (i.e. methane, dimethylsulfide), and the oxidation of elemental mercury. Iodine mainly enters the atmosphere from oceans; therefore, past measurements of atmospheric iodine have focused on marine and polar regions. This study describes the first lower atmospheric measurements of iodine monoxide (IO) radicals at a remote mountaintop site in the central continental United States. These measurements indicate that the concentration of IO radicals showed a large range over the course of one month and reached levels up to three times higher than predicted by a global atmospheric chemistry model. These observations suggest that our understanding of the iodine sources and sinks to the free troposphere may be incomplete. Moreover, we suggest that iodine's contribution to ozone destruction and mercury chemistry may be underestimated; in particular, iodine may be competitive with bromine in the oxidation of elemental mercury in the free troposphere.

1 Introduction

Atmospheric iodine destroys ozone (Read et al., 2008; Saiz-Lopez et al., 2012, 2014; Sherwen et al., 2017; Koenig et al., 2020, 2021), forms new particles (O'Dowd et al. 2002; Sipilä et al., 2016; Baccarini et al., 2020; He et al., 2021; Gómez Martín et al., 2022; Finkenzeller et al., 2023), and modifies atmospheric oxidative capacity (Sherwen et al., 2016a, 2016b). Iodine mainly enters the atmosphere in inorganic gaseous form (HOI, I_2) through reaction with ozone at the ocean surface (Carpenter et al., 2013; MacDonald et al., 2014; Wang et al., 2021), with smaller sources from organic iodine species (Bell et al, 2002; Sive et al., 2007; Jones et al., 2010; Ordóñez et al., 2012; Wang et al., 2021), windblown dust (Williams et al., 2007; Koenig et al., 2021), and volcanic eruptions (Schönhardt et al., 2017). Tree ring and ice core records indicate that atmospheric iodine has increased threefold since 1950, which is attributed to increased anthropogenic surface ozone pollution resulting in increased marine iodine emissions (Legrand et al., 2018; Cuevas et al., 2018; Zhao et al. 2019).

Most of our knowledge about the global distribution of atmospheric iodine is from measurements of iodine monoxide (IO) radicals in the marine boundary layer (Alicke et al., 1999; Allan et al., 2000; Whalley et al., 2007; Furneaux et al., 2010; Coburn et al., 2011;

Mahajan et al., 2012; Gómez Martín et al., 2013; Großmann et al., 2013; Prados-Roman et al., 2015; Inamdar et al., 2020; Takashima et al., 2022) and at high latitudes (Wittrock et al., 2000; Frieß et al., 2010; Mahajan et al., 2010; Schönhardt et al., 2012, 2017). Recent evidence of IO in the free troposphere is limited to measurements over oceans (Puentedura et al., 2012; Dix et al., 2013; Wang et al., 2015; Volkamer et al., 2015; Koenig et al., 2021). IO in the tropical transition layer (Volkamer et al., 2015) and lower stratosphere (Koenig et al., 2020) suggests that iodine is globally distributed. To our knowledge, there is no previous ground-based measurement of tropospheric IO over the continental United States. The only previous attempt to measure IO from the continental U.S. was by Wennberg et al. (1997), who measured IO slant column densities (SCDs) during three sunrises at Kitt Peak, Arizona, with a solar geometry that maximized sensitivity to stratospheric IO but minimized sensitivity to tropospheric IO; they did not attempt to quantify tropospheric IO. Therefore, tropospheric IO over the center of the continental U.S. is unconstrained by ground-based measurements.

Mountaintop Multi-AXis Differential Optical Absorption Spectroscopy (MAX-DOAS) is well-suited for tropospheric IO measurements because it maximizes measurement sensitivity by minimizing aerosol scattering effects, provides access to the free troposphere due to the extended spatial scale (tens of kilometers) of the measurement light path, and enables cost-effective long-term measurements compared to airborne campaigns. Mountaintop MAX-DOAS has been successfully employed for IO measurements in the marine free troposphere (Puentedura et al., 2012).

The role of iodine radicals as oxidants of atmospheric mercury is understudied. Mercury enters the atmosphere mainly in gaseous elemental form, $Hg^0_{(g)}$, where it is oxidized into short-lived $Hg^I(X)_{(g)}$ species (X = Br, OH, Cl) and subsequently reacts with ozone or other secondary oxidants to form $Hg^{II}_{(g)}$ species (Dibble et al., 2020; Shah et al., 2021; Castro et al., 2022). The oxidation of $Hg^0_{(g)}$ by atmospheric iodine radicals has been deemed unimportant due to the low amounts of tropospheric iodine and the much faster thermal decomposition of $Hg^I(I)_{(g)}$ compared to $Hg^I(Br)_{(g)}$ (Goodsite et al., 2004; Shepler et al., 2005; Cremer et al., 2008). Accordingly, the latest implementation of atmospheric mercury chemistry in the GEOS-Chem model does not include reactions involving iodine (Shah et al., 2021). However, mercury measurements in aerosols are empirically correlated with iodine (Murphy et al., 2006). Additionally, the fast, barrierless reaction of Hg^I species with ozone (Saiz-Lopez et al., 2020) can compete with the thermal decomposition of $Hg^I(I)_{(g)}$, prompting us to re-evaluate the importance of iodine as an $Hg^0_{(g)}$ oxidant.

Here we present one month (April 1–30, 2022) of MAX-DOAS measurements of IO, H_2O, NO_2, and HCHO tropospheric vertical column densities (VCD_{trop}) and volume mixing ratios at instrument altitude (VMR_{instr}) alongside co-located in-situ measurements of $Hg^0_{(g)}$ and Hg^{II} at a remote mountaintop observatory in the central continental U.S. Section 2 describes the measurement site and methods. Section 3 presents the first ground-based observational constraint on tropospheric IO over the central continental U.S., explores correlations, and compares observations with a global model. Section 4 uses the observations to constrain a box model of gas-phase mercury chemistry to investigate the relevance of iodine radicals for $Hg^0_{(g)}$ oxidation and discusses atmospheric implications.

2 Methods

2.1 Storm Peak Laboratory

Storm Peak Laboratory (SPL) is a mountaintop observatory on top of the continental divide in the Rocky Mountains in northwestern Colorado (3220 m.a.s.l, 40.455°N, 106.745°W). SPL has been an atmospheric research station since the 1980's (Borys & Wetzel, 1997; Hallar et al., 2016) and has been previously used for atmospheric mercury measurements (Obrist et al., 2008; Fain et al., 2009). All measurements presented here were conducted at SPL from April 1–30, 2022.

2.1.1 CU MAX-DOAS

The University of Colorado MAX-DOAS (CU MAX-DOAS) instrument (Coburn et al., 2011, 2016) measured ultraviolet-visible scattered-light solar spectra at different elevation angles in a single azimuthal viewing direction. Trace gas differential slant column densities (dSCDs) were retrieved from solar spectra using the DOAS method (Platt & Stutz, 2008; Van Roozendael, 2021). A cloud-free zenith reference spectrum (Gielen et al., 2014; Wagner et al., 2014) on April 6, 2022 at 18:00 UTC was used for all DOAS retrievals; fit settings are in Tables S1 & S2. IO, H_2O, HCHO, and O_2-O_2 dSCDs were converted into SCDs by adding the trace gas SCD in the reference spectrum (SCD_{ref}); past studies have shown that accounting for SCD_{ref} maximizes sensitivity in the free troposphere (Hendrick et al., 2007; Coburn et al., 2016) and avoids bias in the retrieval of columns and profiles (Volkamer et al., 2015). For NO_2, the stratospheric signal was removed by subtracting the zenith dSCDs from the off-axis dSCDs. A linear optimal estimation algorithm (Rodgers, 2004) was used to retrieve IO, NO_2, H_2O, and HCHO VCD_{trop} and VMR_{instr} from the measured SCDs (zenith-subtracted dSCDs for NO_2). Instrument and retrieval details are in Text S1.

2.1.2 Dual-channel mercury system

A cation-exchange membrane-based dual-channel system to measure $Hg^0_{(g)}$ and Hg^{II} (Lyman et al., 2020; Elgiar et al., submitted) pulled sample air through a heated PTFE Teflon-coated inlet with an elutriator and particle impactor (2.5 µm cut point), 50 cm of heated PFA Teflon line, to two separate measurement channels. A Tekran 2537X Hg vapor analyzer sampled from each channel sequentially. One channel included a series of two in-series cation exchange-membranes that have been shown to pass $Hg^0_{(g)}$ and retain Hg^{II} (Miller et al., 2019); the other channel included a thermal converter that converted total atmospheric Hg to $Hg^0_{(g)}$. Hg^{II} was calculated as the difference between the two channels every ten minutes.. The dual-channel system had a 1-hour Hg^{II} detection limit less than 15 pg m^{-3}; total Hg and $Hg^0_{(g)}$ are assumed to be similar. A NIST-traceable permeation tube-based calibrator was used to add $Hg^0_{(g)}$ and $HgBr_2$ to the inlet of the dual-channel system while it sampled ambient air, and the system recovered 97±4% and 100±9%, respectively (mean ± standard deviation). The dual-channel system is described in detail in Elgiar et al. (submitted).

2.2 Model tools

2.2.1 GEOS-Chem

The GEOS-Chem 3-D atmospheric chemistry model was used to simulate (1) oxidant fields and (2) mercury chemistry as described in Shah et al. (2021). Details are in Text S2. April 2022 daytime averages of GEOS-Chem oxidant fields and Hg^0 were used to constrain the gas-phase mercury box model described in Section 2.2.3.

2.2.2 HYSPLIT-STILT

The Hybrid Single-Particle Lagrangian Integrated Trajectory (HYSPLIT) model coupled to the Stochastic Time-Inverted Lagrangian Transport Model (STILT; Lin et al., 2003; Loughner et al., 2021) was used to simulate air mass origin at SPL. One thousand 24-hour back trajectories were initiated at each of multiple altitudes (5 m, 2 km, 4 km, 6 km, 10 km above ground level) at SPL every 3 hours from April 1–30, 2022. At each initial altitude, the one thousand back-trajectories were averaged in three dimensions (latitude, longitude, altitude) to calculate a single back trajectory every three hours (Figure 1). Details are in Text S4.

2.2.3 Mercury box model

The Framework for 0-D Atmospheric Modeling (F0AM; Wolfe et al, 2016) version 4.2.2 was used to simulate gas-phase mercury chemistry in 1 km layers from the surface at 2 km to 12 km. GEOS-Chem April 2022 daytime averages were used to constrain oxidant fields and Hg^0; iodine radicals were scaled to the average observed IO column (Text S3). The reaction mechanism used is based on Shah et al. (2021) with three significant differences; first, reactions involving I & IO were added analogously to reactions involving Br & BrO (Saiz-Lopez et al., 2018); second, the reaction coefficient used for $Hg^IX + O_3 \rightarrow Hg^{II}(X)(O) + O_2$ was the value for a barrierless reaction reported in Saiz-Lopez et al. (2020); third, only gas-phase reactions are treated here, as the goal is to examine the relative contributions of Br, OH, and I to $Hg^0_{(g)}$ oxidation rates. $Hg^{II}_{(g)}$ deposition and particle-phase partitioning is not the focus of this study and deemed independent of $Hg^{II}_{(g)}$ chemical identity (Shah et al., 2021). Sensitivity studies were performed varying the rate for $Hg^0 + I + M \rightarrow Hg^I(I) + M$, where a) $Hg^I(I)$ forms at the same rate as $Hg^I(Br)$ and b) $Hg^I(I)$ forms at the rate calculated by Goodsite et al. (2004). The bond strength of $Hg^I(I)$ is uncertain (Goodsite et al., 2004; Shepler et al., 2005; Cremer et al., 2008), and sensitivity studies were performed varying the decomposition rate for $Hg^I(I) + M \rightarrow Hg^0 + I + M$, where a) $Hg^I(I)$ dissociates at the same rate as $Hg^I(OH)$, b) 10 times faster, and c) 100 times faster. Box model output was extracted at fifteen minutes, after gas-phase equilibrium was reached (Figure S3). The complete reaction mechanism is in Tables S5 and S6.

2.2.4 Radiative transfer model

The 3D Monte Carlo Atmospheric Radiative Transfer Inversion Model (McArtim3; Deutschmann et al., 2011) was used to calculate weighting functions for trace gas profile inversions. Model settings are in Table S2. Weighting functions were calculated in a Rayleigh atmosphere using April 2022 average daytime temperature and pressure profiles from ECMWF CAMS reanalysis (Inness et al., 2019) and empirically scaled to match the measured O_2-O_2 SCD for each spectrum. This approach uses the known O_2-O_2 vertical profile to account for the effects of terrain and temporal atmospheric state variability (temperature, pressure, weak aerosols) on the measured photon path distribution (Spinei et al., 2015; Ortega et al., 2016; Wagner et al., 2019; Tirpitz et al., 2021; see Text S1).

3 Results

Here, IO observations are described, compared with GEOS-Chem simulations, and examined alongside co-located observations of air mass tracers for atmospheric dynamics (H_2O), pollution (NO_2), total oxidative capacity (HCHO), and mercury oxidation ($Hg^0_{(g)}$, Hg^{II}). Pearson correlation coefficients (R) of less than 0.20 are referred to as having no correlation; R is reported alongside its standard error. Averages are reported alongside standard deviations.

3.1 Detection of IO in the continental free troposphere

IO concentrations above the detection limit were consistently observed throughout the month; spectral proofs are shown in Figure 1. On April 16, the day with the highest IO signal, IO dSCDs of up to $(2.2\pm0.4)\times10^{13}$ and $(1.6\pm0.1)\times10^{13}$ molec cm^{-2} were observed in the limb (EA=0°) and zenith (EA=90°) geometries, respectively. On April 6, the day with the lowest IO signal, IO dSCDs of up to $(1.4\pm0.4)\times10^{13}$ and $(0.6\pm0.1)\times10^{13}$ molec cm^{-2} were observed in the limb and zenith geometries, respectively.

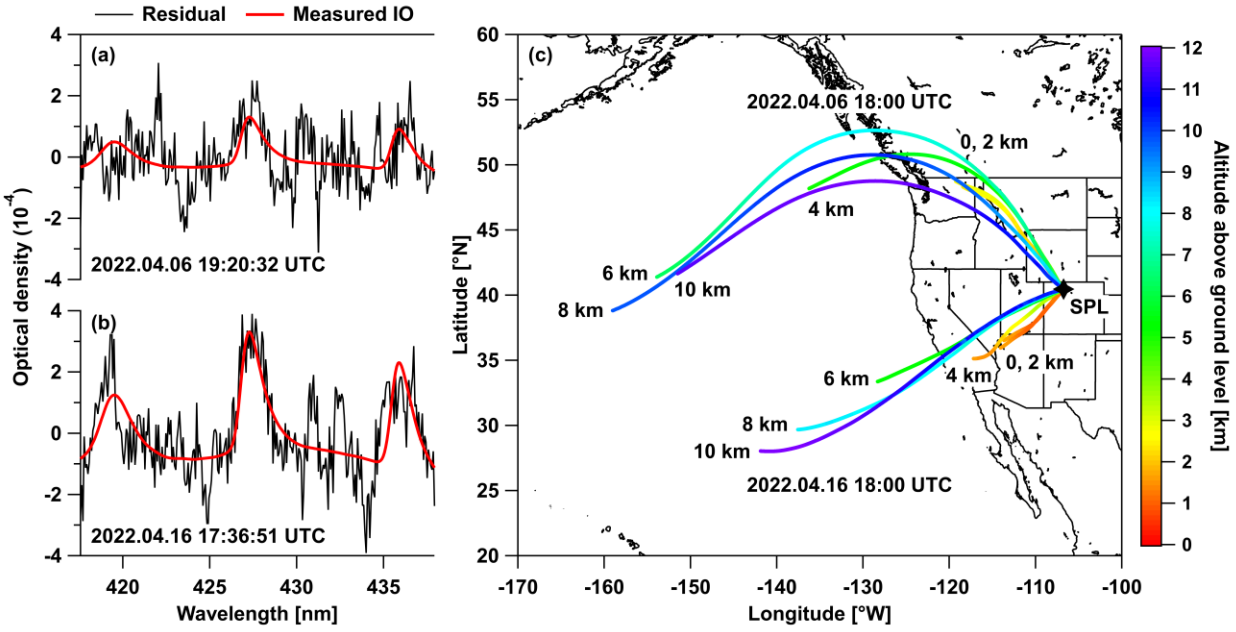

Figure 1. Detection of IO radicals above Storm Peak Laboratory during April 2022. (a) IO spectral proof for a "low IO" case on April 6 at 19:20:32 UTC corresponding to $(0.6\pm0.1)\times10^{13}$ molec cm^{-2} IO dSCD. (b) IO spectral proof for a "high IO" case on April 16 at 17:36:51 UTC corresponding to $(1.6\pm0.1)\times10^{13}$ molec cm^{-2} IO dSCD. (c) Average STILT 24-hour back trajectories for April 6 at 18:00 UTC and April 16 at 18:00 UTC.

Sensitivity studies varying the a priori profile used for the IO column retrieval indicate that IO VMR increased with altitude. Two a priori profiles were tested: a "flat" profile with a constant 0.10 pptv IO throughout the atmosphere, and the GEOS-Chem April 2022 daytime average IO profile. The GEOS-Chem profile, in which IO VMR increases with altitude, consistently resulted in better agreement between measured and a posteriori simulated IO SCDs than the "flat" profile (Figure S2). Therefore, the GEOS-Chem profile was used in the IO retrieval as it is more physically representative of the measurements.

IO VCD_{trop} (VMR_{instr}) was 0.7–3.6×10^{12} molec cm^{-2} (0.00–0.16 pptv), averaging (1.9±0.6)×10^{12} molec cm^{-2} (0.08±0.03 pptv). IO VCD_{trop} (IO VMR_{instr}) error is 0.5×10^{12} molec cm^{-2} (0.03 pptv), with contributions from choice of a priori settings (0.3×10^{12} molec cm^{-2}; 0.01 pptv), uncertainty in SCD_{ref} (0.1×10^{12} molec cm^{-2}; <0.01 pptv), and method error (spectral fitting, radiative transfer modeling, optimal estimation; 0.1×10^{12} molec cm^{-2}; 0.02 pptv). Uncertainty in the IO absorption cross section is 2%, and negligible (Spietz et al., 2005).

24-hour STILT back trajectories indicated that the observed air masses consistently originated from over the Pacific Ocean. The air mass observed during the day with the highest IO signal (April 16) originated from the southwest, towards the tropics (Figure 1c). The air mass observed during the day with the lowest IO signal (April 6) originated from the northwest, towards mid-latitudes. However, not all tropical air masses contained higher IO; on April 28, for example, the back-trajectories indicated an air mass originating even further south than on April 16, yet the IO VCD was significantly larger on April 16 than on April 28. While air mass origin alone cannot account for the observed IO variability, we consistently found higher IO in air masses with less than 24-hour transport time from the Pacific Ocean. This indicated that IO variability also depended on the strength of IO sinks along the transport path, which are not constrained in our analysis.

IO VCD_{trop} and VMR_{instr} were up to three times larger, and the range of IO VCD_{trop} and VMR_{instr} was larger than predicted by GEOS-Chem (Figure 2). GEOS-Chem daytime IO VCD_{trop} (VMR_{instr}) was 0.3–1.5×10^{12} molec cm^{-2} (0.0007–0.10 pptv), averaging 0.8±0.2×10^{12} molec cm^{-2} (0.04±0.02 pptv), two times smaller than observed. There was no correlation between measured and modeled IO VCD_{trop}. There was a very weak but statistically significant anti-correlation between measured and modeled IO VMR_{instr} (R: -0.20±0.05; $p<1\times10^{-4}$). The two days with the lowest IO VCD_{trop}, April 6 and 26, showed reasonable agreement with GEOS-Chem. However, on all other days, IO VCD_{trop} was significantly larger than predicted. The GEOS-Chem horizontal grid cell size (0.5°×0.625°) is comparable to the tens of kilometers sampled by the MAX-DOAS light path. The similar magnitude of underestimation of IO VCD_{trop} and VMR_{instr} by GEOS-Chem provides evidence that IO VMR increased with altitude, since GEOS-Chem consistently simulated increasing IO VMR with altitude. One would expect the GEOS-Chem underestimation to be different between IO VCD_{trop} and VMR_{instr} if the measured profile shape was very different than modeled.

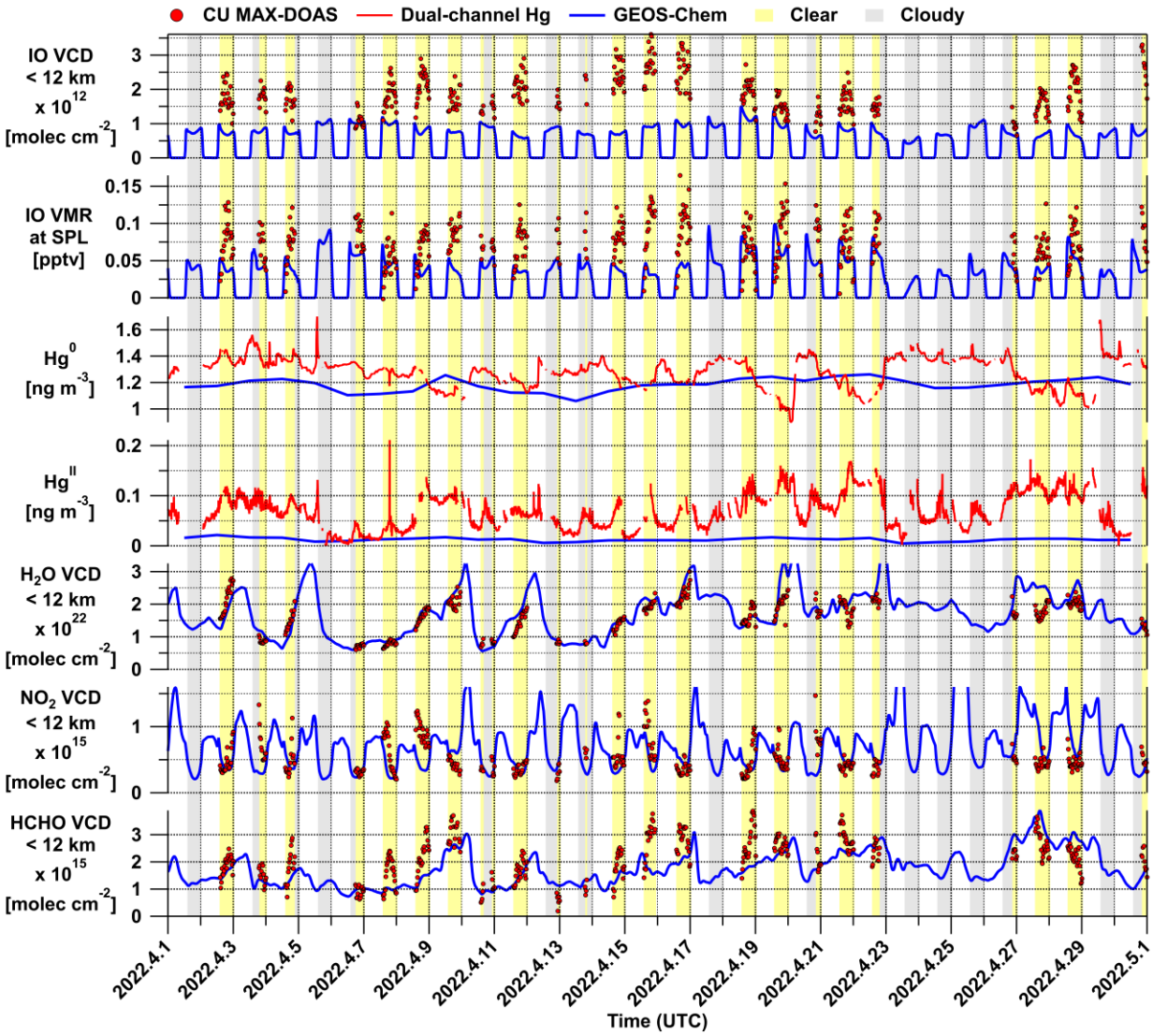

Figure 2. Measurements of IO, Hg^0, Hg^{II}, H_2O, NO_2, and HCHO at Storm Peak Laboratory are compared with GEOS-Chem during April 2022.

3.2 Measurements of other gases at SPL

During April 1–30, 2022 at SPL, GEOS-Chem very accurately simulated both H_2O magnitude and temporal variability; very accurately simulated NO_2 magnitude but failed to simulate NO_2 temporal variability; and accurately simulated HCHO magnitude but had only moderate success in simulating HCHO temporal variability.

3.2.1 H_2O

H_2O VCD_{trop} (VMR_{instr}) was 0.6–3.0×10^{22} molec cm^{-2} (0.4–2.8‰), averaging 1.6±0.5×10^{22} molec cm^{-2} (1.5±0.5 ‰). Total error for H_2O VCD_{trop} (VMR_{instr}) is 0.2×10^{22} molec cm^{-2} (0.1‰). There was no correlation between H_2O VCD_{trop} and IO VCD_{trop}, and a weak correlation between H_2O VMR_{instr} and IO VMR_{instr} (R: 0.35±0.05; $p<1\times10^{-5}$).

GEOS-Chem daytime H_2O VCD_{trop} (VMR_{instr}) is from the MERRA-2 reanalysis and was 0.6–3.8×10^{22} molec cm^{-2} (0.7–6.8‰), averaging 1.7±0.7×10^{22} molec cm^{-2} (3.1±1.2 ‰). The measured and modeled H_2O VCD_{trop} variations were strongly correlated (R: 0.76±0.03; $p<1\times10^{-5}$) and agreed well (Figure 2), indicating model skill in simulating atmospheric H_2O column variability due to passing frontal systems, consistent with earlier observations (Bosilovich et al. 2017). This agreement corroborates control over radiative transfer in the column retrieval method that applies to all trace gas columns presented here.

3.2.2 NO_2

NO_2 VCD_{trop} (VMR_{instr}) was 0.2–1.5×10^{15} molec cm^{-2} (0.01–0.26 ppbv), averaging 0.5±0.2×10^{15} molec cm^{-2} (0.08±0.05 ppbv). Total error for NO_2 VCD_{trop} (VMR_{instr}) is 0.4×10^{15} molec cm^{-2} (0.01 ppbv). There was no correlation between the NO_2 VCD_{trop} and IO VCD_{trop} or between NO_2 VMR_{instr} and IO VMR_{instr}, which is expected due to different sources.

GEOS-Chem daytime NO_2 VCD_{trop} (VMR_{instr}) was 0.2–1.6×10^{15} molec cm^{-2} (0.01–0.24 ppbv), averaging 0.5±0.2×10^{15} molec cm^{-2} (0.07±0.03 ppbv). GEOS-Chem struggled to accurately simulate tropospheric NO_2 at SPL; this is consistent with previously observed model-measurement disagreement in tropospheric NO_2 (Shah et al., 2023). While the range and average for the columns and concentrations closely agree with those observed, there was no correlation between measured and modeled NO_2 VCD_{trop} or VMR_{instr}.

3.2.3 HCHO

HCHO VCD_{trop} (VMR_{instr}) was 0.2–3.9×10^{15} molec cm^{-2} (-0.02–0.67 ppbv), averaging 2.2±0.8×10^{15} molec cm^{-2} (0.36±0.15 ppbv). Total error for HCHO VCD_{trop} (VMR_{instr}) is 0.2×10^{15} molec cm^{-2} (0.03 ppbv). There was no correlation between HCHO VCD_{trop} and IO VCD_{trop}, and a weak correlation between HCHO VMR_{instr} and IO VMR_{instr} (R: 0.31±0.05; $p<1\times10^{-5}$).

GEOS-Chem daytime HCHO VCD_{trop} (VMR_{instr}) was 0.7–3.9×10^{15} molec cm^{-2} (0.0–0.7 ppbv), averaging 1.7±0.6×10^{15} molec cm^{-2} (0.3±0.1 ppbv). The observed HCHO was systematically higher than predicted. The correlation between measured and modeled HCHO VCD_{trop} was moderate (R: 0.57±0.04; $p<1\times10^{-5}$), and a strong correlation was found between measured and modeled HCHO VMR_{instr} (R: 0.66±0.04; $p<1\times10^{-5}$). Overall, the range and average for HCHO VCD_{trop} and VMR_{instr} agree closely with those observed, and the model had better skill in predicting HCHO variability than NO_2 or IO variability at SPL.

3.2.4 BrO

A measurement constraint on bromine was not possible during the study period. The amount of tropospheric BrO observed at SPL was consistently below the detection limit of ~0.5 pptv VMR_{instr}. The GEOS-Chem April 2022 daytime average BrO VMR_{instr} at SPL was 0.15 pptv, consistent with the observations and too low to be observable even with the state-of-the-art MAX-DOAS instrument used here. We therefore used the GEOS-Chem BrO profile without modifications to constrain the mercury box model.

3.3 Mercury

$Hg^0_{(g)}$ (Hg^{II}) was 0.90–1.70 ng m^{-3} (0–211 pg m^{-3}), averaging 1.28±0.11 ng m^{-3} (68±34 pg m^{-3}). Interestingly, there was a weak anti-correlation between $Hg^0_{(g)}$ and HCHO VMR_{instr} (R: -0.35±0.05; $p<1\times10^{-5}$), and a moderately strong correlation between Hg^{II} and HCHO VMR_{instr}

(R: 0.64±0.04; $p<1\times10^{-5}$), indicating a possible connection between mercury oxidation and total atmospheric oxidative capacity.

Oxidized mercury at SPL coincided with warm air masses at low relative humidity, consistent with past work (Fain et al., 2009), but also at high absolute humidity. There was a weak anti-correlation between $Hg^0_{(g)}$ and measured temperature (R: -0.37±0.02; $p<1\times10^{-5}$), a strong correlation between Hg^{II} and measured temperature (R: 0.70±0.01; $p<1\times10^{-5}$), a weak correlation between $Hg^0_{(g)}$ and measured relative humidity (R: 0.39±0.02; $p<1\times10^{-5}$), a moderate anti-correlation between Hg^{II} and measured relative humidity (R: -0.43±0.01; $p<1\times10^{-5}$), and a weak correlation between Hg^{II} and H_2O VMR_{instr} (R: 0.37±0.04; $p<1\times10^{-5}$). This is consistent with the idea that mercury survives longer in air masses with less wet deposition, providing more time for oxidation to occur.

GEOS-Chem $Hg^0_{(g)}$ (Hg^{II}) was 1.06–1.26 ng m^{-3} (4–22 pg m^{-3}), averaging 1.18±0.05 ng m^{-3} (12±4 pg m^{-3}). While measured and modeled Hg^0 concentrations agreed reasonably well, there was no correlation in Hg^0 temporal variability. Moreover, the measured Hg^{II} concentration was up to ten times larger and more variable (i.e., a six times larger standard deviation) than modeled (Figure 2). Despite these differences, measured and modeled Hg^{II} were moderately correlated (R: 0.47±0.01; $p<1\times10^{-5}$), indicating that GEOS-Chem had some skill in predicting Hg^{II} variability at SPL but not the magnitude. Increased Hg^{II} sources (i.e., iodine-induced oxidation) and/or decreased Hg^{II} sinks in the model are needed to explain this model-measurement disagreement.

4 Discussion

4.1 Literature comparison

The observed IO VCD_{trop} monthly average of $1.9\pm0.6\times10^{12}$ molec cm^{-2} over the central continental U.S. is consistent with the few previous airborne measurements. Dix et al. (2013) reported an IO VCD_{trop} of 2.49 to 2.91×10^{12} molec cm^{-2} over the central Pacific and Volkamer et al. (2015) found 2.1 to 2.5×10^{12} molec cm^{-2} over the eastern Pacific; both studies probed tropical air in the northern hemisphere winter. The average IO VCD_{trop} above SPL demonstrates that iodine is widespread in the free troposphere, including over continents.

The significant day-to-day temporal variability in IO VCD_{trop} over the central continental U.S. (0.7±0.5 to $3.6\pm0.5\times10^{12}$ molec cm^{-2}) has not been previously observed. Our measurements also characterize IO VCD_{trop} for the first time in the spring. Information about iodine spatiotemporal variability in the free troposphere is extremely scarce. Two sources affecting free tropospheric IO variability are marine convection (Dix et al., 2013) and dust (Puentedura et al., 2012; Koenig et al., 2021). Regional-scale IO variability over the Eastern Pacific Ocean was systematically probed by Wang et al. (2015), who reported IO VCD_{trop} of 2.6 to 3.5×10^{12} molec cm^{-2} and 5.1×10^{12} molec cm^{-2} in the southern hemisphere tropical and subtropical Pacific, respectively, during Austral summer. Some of this variability could be attributed to dust sources of iodine from the Sechura and Atacama deserts (Koenig et al., 2021), with regional impacts on ozone in the marine boundary layer and free troposphere. Puentedura et al. (2012) reported variability in IO dSCDs related to Saharan dust impacts in the free troposphere over Tenerife Island in the Eastern Atlantic; they did not attempt to retrieve IO VCD_{trop}. Elevated IO VCD_{trop} over SPL is related to rapid transport from the Pacific Ocean, consistent with marine convection upwind, and unrelated to immediate dust impacts.

Schönhardt et al. (2008) reported global satellite measurements of IO SCDs. Their analysis used a reference spectrum over the tropical Pacific, where airborne measurements indicate that there is a significant IO VCD_{trop} (Dix et al., 2013; Volkamer et al., 2015). Therefore, the satellite IO SCDs are lower limits and not directly comparable to our measurements.

4.2 Ozone relevance

Iodine is responsible for a ~9% reduction in the total tropospheric ozone burden, and model-measurement agreement for IO profiles over the eastern tropical Pacific indicates that marine sources for IO are reasonably well-constrained (Wang et al., 2021). The consistent low bias in modeled IO compared to our observations suggests that iodine's contribution to tropospheric ozone destruction may be higher than currently estimated over continents. In particular, GEOS-Chem iodine chemistry has not been significantly updated since version 11-02-rc, with the implementation of Wang et al. (2021) in version 12.9 leaving the mechanism of Sherwen et al. (2016b) largely unchanged.

4.3 Implications for atmospheric mercury oxidation

Iodine oxidation of mercury is deemed unimportant, and is therefore missing in atmospheric models, in part due to the lower Hg-I bond strength (8.3–10.9 kcal mol^{-1}) compared to Hg-Br (14.4–17.9 kcal mol^{-1}) and Hg-OH (9.4–12.4 kcal mol^{-1}) (Goodsite et al., 2004; Shepler et al., 2005; Cremer et al., 2008; Dibble et al., 2020). The Hg-OH bond strength was previously thought to be too weak to lead to Hg^{II} formation, but the discovery that the reaction of Hg^{I} species with ozone is kinetically barrierless (Saiz-Lopez et al., 2020) has resulted in a re-evaluation of the global relevance of OH radicals to $Hg^{0}_{(g)}$ oxidation (Shah et al., 2021; Castro et al., 2022; Hewa Edirappulige et al., 2023). There is evidence suggesting that the reaction of $Hg^{0}_{(g)}$ with I atom proceeds faster than with Br atom (Goodsite et al., 2004). In light of the larger than predicted amounts of tropospheric iodine over continents, the Hg-I bond strength and $Hg^{I}(I)_{(g)}$ dissociation rate warrant re-evaluation.

Our box model results (Figure 3) show that I atoms may oxidize Hg^{0} at rates rivaling Br atoms at cold temperatures typical of the free troposphere (4–12 km; <260K). Above 9 km, this finding is independent of the assumed Hg-I bond strength, as $Hg^{I}(I)_{(g)}$ dissociation is slow at cold temperatures. Below 9 km, iodine-induced Hg oxidation may rival Br depending on the assumed Hg-I bond strength, which is highly uncertain. Our most conservative estimate, which uses the Hg+Br kinetics measured by Donohoue et al. (2006) for the Hg+I reaction and assumes that $Hg^{I}(I)$ dissociates 100 times faster than $Hg^{I}(OH)$, places iodine atoms at a contribution of 1.2%–42.1% to $Hg^{II}_{(g)}$ formation below 12 km (Br: 17.4–68.3%; OH: 7.6–81.1%; Cl: <0.5%). Our least conservative estimate, which uses the bimolecular rate constant calculated by Goodsite et al. (2004) for the Hg+I reaction and assumes that $Hg^{I}(I)$ dissociates at the same rate as $Hg^{I}(OH)$, places iodine atoms at a contribution of 40.1–78.7% to $Hg^{II}_{(g)}$ formation below 12 km (Br: 12.4–46.9%; OH: 6.4–57.8%; Cl: <0.5%). These results are consistent with the observed correlation between mercury and iodine in aerosols in the lower stratosphere (Murphy et al., 2006), and suggest these correlations might have a mechanistic causal relationship. The inclusion of iodine radical oxidation of $Hg^{0}_{(g)}$ to Hg^{II} in atmospheric models is desirable and will benefit from better knowledge of the chemical kinetics, from laboratory experiments and calculations, and better constraints on the tropospheric iodine distribution.

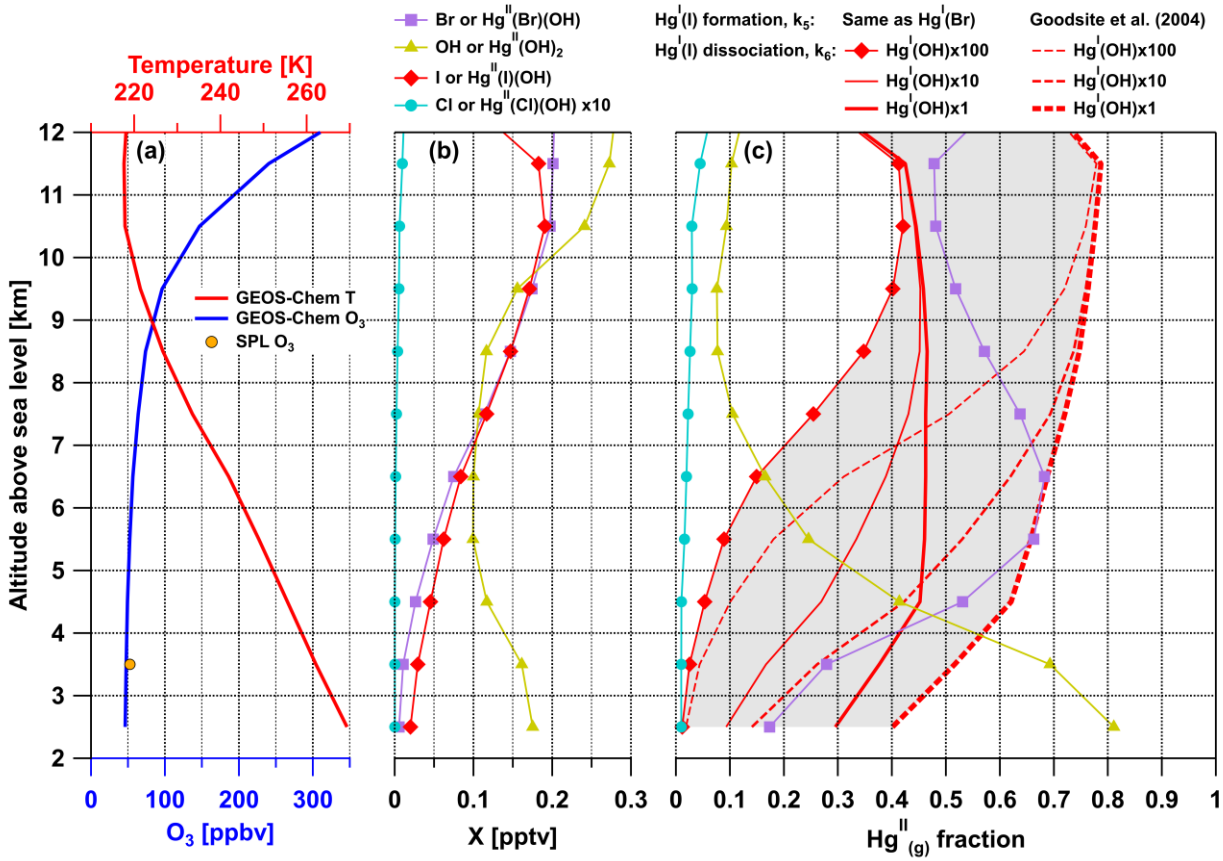

Figure 3. Iodine-initiated Hg^0 oxidation compared with other radical pathways above Storm Peak Laboratory. Iodine appears to be a competitive oxidant throughout the troposphere and becomes more relevant at colder temperatures in the upper free troposphere. See Section 2.2.3, Section 4.3, Text S3, Table S5, and Table S6 for details.

Acknowledgments

Funding from the U.S. National Science Foundation (AGS-1951513, AGS-1951514, AGS-1951515, AGS-1951632) is gratefully acknowledged. The Steamboat Ski Resort, Maria Garcia, Dan Gilchrist, and SPL staff provided logistical support. Caroline Womack and Jessica Haskins assisted with F0AM. The Global Modeling and Assimilation Office at NASA Goddard Space Flight Center provided MERRA-2 meteorological data.

Data availability statement

All CU MAX-DOAS and dual-channel mercury system measurement data at Storm Peak Laboratory during April 2022 (measured and GEOS-Chem simulated trace gas SCD, VCD_{trop},

VMR_{instr}; measured and GEOS-Chem simulated Hg^0 & Hg^{II}) as well as the gas-phase mercury chemical box model constraints & output described in this study are publicly available at zenodo via https://zenodo.org/doi/10.5281/zenodo.10805549 with a Creative Commons Attribution 4.0 license. The HYSPLIT-STILT back trajectory simulations at Storm Peak Laboratory during April 2022 described in this study are publicly available at zenodo via https://doi.org/10.5281/zenodo.10806478 with a Creative Commons Attribution 4.0 license. The long-term measurements of Hg^0, Hg^{II}, trace gases, and meteorology at Storm Peak Laboratory, a subset of which are used in this study, are publicly available at zenodo via https://doi.org/10.5281/zenodo.10699270 with a Creative Commons Attribution 4.0 license. Version 13.2.1 of the GEOS-Chem model was used to simulate atmospheric oxidant fields, is preserved at https://doi.org/10.5281/zenodo.5500717, is available via an MIT license, and is developed openly at https://github.com/geoschem/GCClassic/tree/13.2.1. Version 12.8.0 of the GEOS-Chem model was used to simulate atmospheric mercury chemistry, is preserved at https://doi.org/10.5281/zenodo.3784796, is available via an MIT license, and is developed openly at https://github.com/geoschem/geos-chem/tree/12.8.0. Version 3.4.5 of the QDOAS spectral analysis software developed by the DOAS UV-VIS team at the Royal Belgian Institute for Space Aeronomy (BIRA-IASB) was used for all DOAS spectral analysis, is available via a BSD 3-clause type license, and is developed openly at https://github.com/UVVIS-BIRA-IASB/qdoas. Version 8.0.4.2 of the IGOR Pro software developed by WaveMetrics, Inc. was used for data analysis and is available via a commercial license at https://www.wavemetrics.com/products/igorpro. Vector map data of coastlines and state borders used in Panel (c) of Figure 1 are available at Natural Earth via https://www.naturalearthdata.com/ with a public domain license.

References

Alicke, B., Hebestreit, K., Stutz, J., & Platt, U. (1999). Iodine oxide in the marine boundary layer. *Nature*, 397(6720), 572–573. https://doi.org/10.1038/17508

Allan, B. J., McFiggans, G., Plane, J. M. C., & Coe, H. (2000). Observations of iodine monoxide in the remote marine boundary layer. *Journal of Geophysical Research: Atmospheres*, 105(D11), 14363–14369. https://doi.org/10.1029/1999JD901188

Baccarini, A., Karlsson, L., Dommen, J., Duplessis, P., Vüllers, J., Brooks, I. M., Saiz-Lopez, A., Salter, M., Tjernström, M., Baltensperger, U., Zieger, P., & Schmale, J. (2020). Frequent new particle formation over the high Arctic pack ice by enhanced iodine emissions. *Nature Communications*, 11(1), 4924. https://doi.org/10.1038/s41467-020-18551-0

Bell, N., Hsu, L., Jacob, D. J., Schultz, M. G., Blake, D. R., Butler, J. H., King, D. B., Lobert, J. M., & Maier-Reimer, E. (2002). Methyl iodide: Atmospheric budget and use as a tracer of marine convection in global models. *Journal of Geophysical Research: Atmospheres*, 107(D17), 4340. https://doi.org/10.1029/2001JD001151

Borys, R. D., & Wetzel, M. A. (1997). Storm Peak Laboratory: A Research, Teaching, and Service Facility for the Atmospheric Sciences. *Bulletin of the American Meteorological Society*, 78(10), 2115–2123. https://doi.org/10.1175/1520-0477(1997)078%3C2115:SPLART%3E2.0.CO;2

Bosilovich, M. G., Robertson, F. R., Takacs, L., Molod, A., & Mocko, D. (2017). Atmospheric Water Balance and Variability in the MERRA-2 Reanalysis. *Journal of Climate*, 30(4), 1177–1196. https://doi.org/10.1175/JCLI-D-16-0338.1

Carpenter, L. J., MacDonald, S. M., Shaw, M. D., Kumar, R., Saunders, R. W., Parthipan, R., Wilson, J., & Plane, J. M. C. (2013). Atmospheric iodine levels influenced by sea surface

emissions of inorganic iodine. *Nature Geoscience*, 6(2), 108–111. https://doi.org/10.1038/ngeo1687

Castro, P. J., Kellö, V., Cernušák, I., & Dibble, T. S. (2022). Together, Not Separately, OH and O_3 Oxidize $Hg^{(0)}$ to $Hg^{(II)}$ in the Atmosphere. *The Journal of Physical Chemistry A*, 126(44), 8266–8279. https://doi.org/10.1021/acs.jpca.2c04364

Coburn, S., Dix, B., Edgerton, E., Holmes, C. D., Kinnison, D., Liang, Q., ter Schure, A., Wang, S., & Volkamer, R. (2016). Mercury oxidation from bromine chemistry in the free troposphere over the southeastern US. *Atmospheric Chemistry and Physics*, 16(6), 3743–3760. https://doi.org/10.5194/acp-16-3743-2016

Coburn, S., Dix, B., Sinreich, R., & Volkamer, R. (2011). The CU ground MAX-DOAS instrument: characterization of RMS noise limitations and first measurements near Pensacola, FL of BrO, IO, and CHOCHO. *Atmospheric Measurement Techniques*, 4(11), 2421–2439. https://doi.org/10.5194/amt-4-2421-2011

Cremer, D., Kraka, E., & Filatov, M. (2008). Bonding in Mercury Molecules Described by the Normalized Elimination of the Small Component and Coupled Cluster Theory. *ChemPhysChem*, 9(17), 2510–2521. https://doi.org/10.1002/cphc.200800510

Cuevas, C. A., Maffezzoli, N., Corella, J. P., Spolaor, A., Vallelonga, P., Kjær, H. A., Simonsen, M., Winstrup, M., Vinther, B., Horvat, C., Fernandez, R. P., Kinnison, D., Lamarque, J.-F., Barbante, C., & Saiz-Lopez, A. (2018). Rapid increase in atmospheric iodine levels in the North Atlantic since the mid-20th century. *Nature Communications*, 9(1), 1452. https://doi.org/10.1038/s41467-018-03756-1

Deutschmann, T., Beirle, S., Frieß, U., Grzegorski, M., Kern, C., Kritten, L., Platt, U., Prados-Román, C., Pukīte, J., Wagner, T., Werner, B., & Pfeilsticker, K. (2011). The Monte

Carlo atmospheric radiative transfer model McArtim: Introduction and validation of Jacobians and 3D features. *Journal of Quantitative Spectroscopy and Radiative Transfer*, 112(6), 1119–1137. https://doi.org/10.1016/j.jqsrt.2010.12.009

Dibble, T. S., Tetu, H. L., Jiao, Y., Thackray, C. P., & Jacob, D. J. (2020). Modeling the OH-Initiated Oxidation of Mercury in the Global Atmosphere without Violating Physical Laws. *The Journal of Physical Chemistry A*, 124(2), 444–453. https://doi.org/10.1021/acs.jpca.9b10121

Dix, B., Baidar, S., Bresch, J. F., Hall, S. R., Schmidt, K. S., Wang, S., & Volkamer, R. (2013). Detection of iodine monoxide in the tropical free troposphere. *Proceedings of the National Academy of Sciences*, 110(6), 2035–2040. https://doi.org/10.1073/pnas.1212386110

Donohoue, D. L., Bauer, D., Cossairt, B., & Hynes, A. J. (2006). Temperature and Pressure Dependent Rate Coefficients for the Reaction of Hg with Br and the Reaction of Br with Br: A Pulsed Laser Photolysis-Pulsed Laser Induced Fluorescence Study. *The Journal of Physical Chemistry A*, 110(21), 6623–6632. https://doi.org/10.1021/jp054688j

Elgiar, T. R., Lyman, S. N., O'Neil, T., Gratz, L. E., Nair, S. V., Živković, I., Horvat, M., Andron, T. D., & Hallar, G. (in preparation). NIST-Traceable Calibration of Atmospheric Oxidized Mercury Measurements.

Faïn, X., Obrist, D., Hallar, A. G., McCubbin, I., & Rahn, T. (2009). High levels of reactive gaseous mercury observed at a high elevation research laboratory in the Rocky Mountains. *Atmospheric Chemistry and Physics*, 9(20), 8049–8060. https://doi.org/10.5194/acp-9-8049-2009

Gratz, L. E., Lyman, S. N., Elgiar, T., Hallar, A. G., & Volkamer, R. (2024). Measurements of atmospheric mercury, trace gases, aerosols, and meteorology at Storm Peak Laboratory, Colorado, in 2021 and 2022 (version 1) [Dataset]. Zenodo. https://doi.org/10.5281/zenodo.10699270

Finkenzeller, H., Iyer, S., He, X.-C., Simon, M., Koenig, T. K., Lee, C. F., Valiev, R., Hofbauer, V., Amorim, A., Baalbaki, R., Baccarini, A., Beck, L., Bell, D. M., Caudillo, L., Chen, D., Chiu, R., Chu, B., Dada, L., Duplissy, J., Heinritzi, M., Kemppainen, D., Kim, C., Krechmer, J., Kürten, A., Kvashnin, A., Lamkaddam, H., Lee, C. P., Lehtipalo, K., Li, Z., Makhmutov, V., Manninen, H. E., Marie, G., Marten, R., Mauldin, R. L., Mentler, B., Müller, T., Petäjä, T., Philippov, M., Ranjithkumar, A., Rörup, B., Shen, J., Stolzenburg, D., Tauber, C., Tham, Y. J., Tomé, A., Vazquez-Pufleau, M., Wagner, A. C., Wang, D. S., Wang, M., Wang, Y., Weber, S. K., Nie, W., Wu, Y., Xiao, M., Ye, Q., Zauner-Wieczorek, M., Hansel, A., Baltensperger, U., Brioude, J., Curtius, J., Donahue, N. M., El Haddad, I., Flagan, R. C., Kulmala, M., Kirkby, J., Sipilä, M., Worsnop, D. R., Kurten, T., Rissanen, M. & Volkamer, R. (2023). The gas-phase formation mechanism of iodic acid as an atmospheric aerosol source. *Nature Chemistry*, 15(1), 129–135. https://doi.org/10.1038/s41557-022-01067-z

Frieß, U., Deutschmann, T., Gilfedder, B. S., Weller, R., & Platt, U. (2010). Iodine monoxide in the Antarctic snowpack. *Atmospheric Chemistry and Physics*, 10(5), 2439–2456. https://doi.org/10.5194/acp-10-2439-2010

Furneaux, K. L., Whalley, L. K., Heard, D. E., Atkinson, H. M., Bloss, W. J., Flynn, M. J., Gallagher, M. W., Ingham, T., Kramer, L., Lee, J. D., Leigh, R., McFiggans, G. B., Mahajan, A. S., Monks, P. S., Oetjen, H., Plane, J. M. C., & Whitehead, J. D. (2010).

518 Measurements of iodine monoxide at a semi polluted coastal location. *Atmospheric*
519 *Chemistry and Physics*, 10(8), 3645–3663. https://doi.org/10.5194/acp-10-3645-2010
520 Gielen, C., van Roozendael, M., Hendrick, F., Pinardi, G., Vlemmix, T., de Bock, V., de Backer,
521 H., Fayt, C., Hermans, C., Gillotay, D., & Wang, P. (2014). A simple and versatile cloud-
522 screening method for MAX-DOAS retrievals. *Atmospheric Measurement Techniques*,
523 7(10), 3509–3527. https://doi.org/10.5194/amt-7-3509-2014
524 Goddard Earth Observing System (GEOS) global 3-D model of atmospheric chemistry.
525 geoschem/GCClassic: GEOS-Chem 12.8.0 [Software]. Zenodo.
526 https://doi.org/10.5281/zenodo.3784796
527 Goddard Earth Observing System (GEOS) global 3-D model of atmospheric chemistry.
528 geoschem/GCClassic: GEOS-Chem 13.2.1 [Software]. Zenodo.
529 https://doi.org/10.5281/zenodo.5500717
530 Gómez Martín, J. C., Lewis, T. R., James, A. D., Saiz-Lopez, A., & Plane, J. M. C. (2022).
531 Insights into the Chemistry of Iodine New Particle Formation: The Role of Iodine Oxides
532 and the Source of Iodic Acid. *Journal of the American Chemical Society*, 144(21), 9240–
533 9253. https://doi.org/10.1021/jacs.1c12957
534 Gómez Martín, J. C., Mahajan, A. S., Hay, T. D., Prados-Román, C., Ordóñez, C., MacDonald,
535 S. M., Plane, J. M. C., Sorribas, M., Gil, M., Paredes Mora, J. F., Agama Reyes, M. v.,
536 Oram, D. E., Leedham, E., & Saiz-Lopez, A. (2013). Iodine chemistry in the eastern
537 Pacific marine boundary layer. *Journal of Geophysical Research: Atmospheres*, 118(2),
538 887–904. https://doi.org/10.1002/jgrd.50132
539 Großmann, K., Frieß, U., Peters, E., Wittrock, F., Lampel, J., Yilmaz, S., Tschritter, J.,
540 Sommariva, R., von Glasow, R., Quack, B., Krüger, K., Pfeilsticker, K., & Platt, U.

(2013). Iodine monoxide in the Western Pacific marine boundary layer. *Atmospheric Chemistry and Physics*, 13(6), 3363–3378. https://doi.org/10.5194/acp-13-3363-2013

Goodsite, M. E., Plane, J. M. C., & Skov, H. (2004). A Theoretical Study of the Oxidation of Hg^0 to $HgBr_2$ in the Troposphere. *Environmental Science & Technology*, 38(6), 1772–1776. https://doi.org/10.1021/es034680s

Hallar, A. G., Petersen, R., McCubbin, I. B., Lowenthal, D., Lee, S., Andrews, E., & Yu, F. (2016). Climatology of New Particle Formation and Corresponding Precursors at Storm Peak Laboratory. *Aerosol and Air Quality Research*, 16(3), 816–826. https://doi.org/10.4209/aaqr.2015.05.0341

Hendrick, F., van Roozendael, M., Chipperfield, M. P., Dorf, M., Goutail, F., Yang, X., Fayt, C., Hermans, C., Pfeilsticker, K., Pommereau, J.-P., Pyle, J. A., Theys, N., & de Mazière, M. (2007). Retrieval of stratospheric and tropospheric BrO profiles and columns using ground-based zenith-sky DOAS observations at Harestua, 60° N. *Atmospheric Chemistry and Physics*, 7(18), 4869–4885. https://doi.org/10.5194/acp-7-4869-2007

Hewa Edirappulige, D. T., Kirby, I. J., Beckett, C. K., & Dibble, T. S. (2023). Atmospheric Chemistry of $HOHg^{(II)}O^{\bullet}$ Mimics That of a Hydroxyl Radical. *The Journal of Physical Chemistry A*, 127(40), 8392–8403. https://doi.org/10.1021/acs.jpca.3c04159

He, X.-C., Tham, Y. J., Dada, L., Wang, M., Finkenzeller, H., Stolzenburg, D., Iyer, S., Simon, M., Kürten, A., Shen, J., Rörup, B., Rissanen, M., Schobesberger, S., Baalbaki, R., Wang, D. S., Koenig, T. K., Jokinen, T., Sarnela, N., Beck, L. J., Almeida, J., Amanatidis, S., Amorim, A., Ataei, F., Baccarini, A., Bertozzi, B., Bianchi, F., Brilke, S., Caudillo, L., Chen, D., Chiu, R., Chu, B., Dias, A., Ding, A., Dommen, J., Duplissy, J., El Haddad, I., Gonzalez Carracedo, L., Granzin, M., Hansel, A., Heinritzi, M., Hofbauer, V., Junninen,

H., Kangasluoma, J., Kemppainen, D., Kim, C., Kong, W., Krechmer J. E., Kvashin, A., Laitinen, T., Lamkaddam, H., Lee, C. P., Lehtipalo, K., Leiminger, M., Li, Z., Makhmutov, V., Manninen, H. E., Marie, G., Marten, R., Mathot, S., Mauldin, R. L., Mentler, B., Möhler, O., Müller, T., Nie, W., Onnela, A., Petäjä, T., Pfeifer, J., Philippov, M., Ranjithkumar, A., Saiz-Lopez, A., Salma, I., Scholz, W., Schuchmann, S., Schulze, B., Steiner, G., Stozhkov, Y., Tauber, C., Tomé, A., Thakur, R. C., Väisänen, O., Vazquez-Pufleau, M., Wagner, A. C., Wang, Y., Weber, S. K., Winkler, P. M., Wu, Y., Xiao, M., Yan, C., Ye, Q., Ylisirniö, A., Zauner-Wieczorek, M., Zha, Q., Zhou, P., Flagan, R. C., Curtius, J., Baltensperger, U., Kulmala, M., Kerminen, V.-M., Kurtén, T., Donahue, N. M., Volkamer, R., Kirkby, J., Worsnop, D. R., Sipilä, M. (2021). Role of iodine oxoacids in atmospheric aerosol nucleation. *Science*, 371(6529), 589–595. https://doi.org/10.1126/science.abe0298

Inamdar, S., Tinel, L., Chance, R., Carpenter, L. J., Sabu, P., Chacko, R., Tripathy, S. C., Kerkar, A. U., Sinha, A. K., Bhaskar, P. V., Sarkar, A., Roy, R., Sherwen, T., Cuevas, C., Saiz-Lopez, A., Ram, K., & Mahajan, A. S. (2020). Estimation of reactive inorganic iodine fluxes in the Indian and Southern Ocean marine boundary layer. *Atmospheric Chemistry and Physics*, 20(20), 12093–12114. https://doi.org/10.5194/acp-20-12093-2020

Inness, A., Ades, M., Agustí-Panareda, A., Barré, J., Benedictow, A., Blechschmidt, A.-M., Dominguez, J. J., Engelen, R., Eskes, H., Flemming, J., Huijnen, V., Jones, L., Kipling, Z., Massart, S., Parrington, M., Peuch, V.-H., Razinger, M., Remy, S., Schulz, M., & Suttie, M. (2019). The CAMS reanalysis of atmospheric composition. Atmospheric Chemistry and Physics, 19(6), 3515–3556. https://doi.org/10.5194/acp-19-3515-2019

Jones, C. E., Hornsby, K. E., Sommariva, R., Dunk, R. M., von Glasow, R., McFiggans, G., & Carpenter, L. J. (2010). Quantifying the contribution of marine organic gases to atmospheric iodine. *Geophysical Research Letters*, 37(18). https://doi.org/10.1029/2010GL043990

Koenig, T. K., Baidar, S., Campuzano-Jost, P., Cuevas, C. A., Dix, B., Fernandez, R. P., Guo, H., Hall, S. R., Kinnison, D., Nault, B. A., Ullmann, K., Jimenez, J. L., Saiz-Lopez, A., & Volkamer, R. (2020). Quantitative detection of iodine in the stratosphere. *Proceedings of the National Academy of Sciences*, 117(4), 1860–1866. https://doi.org/10.1073/pnas.1916828117

Koenig, T. K., Volkamer, R., Apel, E. C., Bresch, J. F., Cuevas, C. A., Dix, B., Eloranta, E. W., Fernandez, R. P., Hall, S. R., Hornbrook, R. S., Pierce, R. B., Reeves, J. M., Saiz-Lopez, A., & Ullmann, K. (2021). Ozone depletion due to dust release of iodine in the free troposphere. *Science Advances*, 7(52), 6544. https://doi.org/10.1126/sciadv.abj6544

Lee, C. F., Elgiar, T., David, L. M., Wilmot, K., Reza, M., Hirshorn, N., McCubbin, I. B., Shah, V., Lin, J. C., Lyman, S. N., Hallar, A. G., Gratz, L. E., & Volkamer, R. (2024). Measurements and model simulations of iodine monoxide (IO) radical, water vapor (H2O), nitrogen dioxide (NO2) radical, formaldehyde (HCHO), gaseous elemental mercury (Hg0), and oxidized mercury (HgII) at Storm Peak Laboratory, Colorado, during April 2022 (Version 1) [Dataset]. Zenodo. https://doi.org/10.5281/zenodo.10805550

Lee, C. F., Wilmot, K., Lin, J. C., Lyman, S. N., Hallar, A. G., Gratz, L. E., & Volkamer, R. (2024). 24-hour HYSPLIT-STILT back-trajectories initialized at Storm Peak Laboratory, Colorado from April 1, 2022 to May 1, 2022 (Version 1) [Dataset]. Zenodo. https://doi.org/10.5281/zenodo.10806478

Legrand, M., McConnell, J. R., Preunkert, S., Arienzo, M., Chellman, N., Gleason, K., Sherwen, T., Evans, M. J., & Carpenter, L. J. (2018). Alpine ice evidence of a three-fold increase in atmospheric iodine deposition since 1950 in Europe due to increasing oceanic emissions. *Proceedings of the National Academy of Sciences*, 115(48), 12136–12141. https://doi.org/10.1073/pnas.1809867115

Lin, J. C., Gerbig, C., Wofsy, S. C., Andrews, A. E., Daube, B. C., Davis, K. J., & Grainger, C. A. (2003). A near-field tool for simulating the upstream influence of atmospheric observations: The Stochastic Time-Inverted Lagrangian Transport (STILT) model. *Journal of Geophysical Research: Atmospheres*, 108(D16). https://doi.org/10.1029/2002JD003161

Loughner, C. P., Fasoli, B., Stein, A. F., & Lin, J. C. (2021). Incorporating features from the Stochastic Time-Inverted Lagrangian Transport (STILT) model into the Hybrid Single-Particle Lagrangian Integrated Trajectory (HYSPLIT) model: a unified dispersion model for time-forward and time-reversed applications. *Journal of Applied Meteorology and Climatology*, 60(6), 799–810. https://doi.org/10.1175/JAMC-D-20-0158.1

Lyman, S. N., Gratz, L. E., Dunham-Cheatham, S. M., Gustin, M. S., & Luippold, A. (2020). Improvements to the Accuracy of Atmospheric Oxidized Mercury Measurements. *Environmental Science & Technology*, 54(21), 13379–13388. https://doi.org/10.1021/acs.est.0c02747

MacDonald, S. M., Gómez Martín, J. C., Chance, R., Warriner, S., Saiz-Lopez, A., Carpenter, L. J., & Plane, J. M. C. (2014). A laboratory characterisation of inorganic iodine emissions from the sea surface: dependence on oceanic variables and parameterisation for global

631 modelling. *Atmospheric Chemistry and Physics*, 14(11), 5841–5852.
632 https://doi.org/10.5194/acp-14-5841-2014
633 Mahajan, A. S., Gómez Martín, J. C., Hay, T. D., Royer, S.-J., Yvon-Lewis, S., Liu, Y., Hu, L.,
634 Prados-Roman, C., Ordóñez, C., Plane, J. M. C., & Saiz-Lopez, A. (2012). Latitudinal
635 distribution of reactive iodine in the Eastern Pacific and its link to open ocean sources.
636 *Atmospheric Chemistry and Physics*, 12(23), 11609–11617. https://doi.org/10.5194/acp-
637 12-11609-2012
638 Mahajan, A. S., Shaw, M., Oetjen, H., Hornsby, K. E., Carpenter, L. J., Kaleschke, L., Tian-
639 Kunze, X., Lee, J. D., Moller, S. J., Edwards, P., Commane, R., Ingham, T., Heard, D. E.,
640 & Plane, J. M. C. (2010). Evidence of reactive iodine chemistry in the Arctic boundary
641 layer. *Journal of Geophysical Research: Atmospheres*, 115(D20).
642 https://doi.org/10.1029/2009JD013665
643 Miller, M. B., Dunham-Cheatham, S. M., Gustin, M. S., & Edwards, G. C. (2019). Evaluation of
644 cation exchange membrane performance under exposure to high Hg^0 and $HgBr^2$
645 concentrations. *Atmospheric Measurement Techniques*, 12(2), 1207–1217.
646 https://doi.org/10.5194/amt-12-1207-2019
647 Murphy, D. M., Hudson, P. K., Thomson, D. S., Sheridan, P. J., & Wilson, J. C. (2006).
648 Observations of Mercury-Containing Aerosols. *Environmental Science & Technology*,
649 40(10), 3163–3167. https://doi.org/10.1021/es052385x
650 Obrist, D., Hallar, A. G., McCubbin, I., Stephens, B. B., & Rahn, T. (2008). Atmospheric
651 mercury concentrations at Storm Peak Laboratory in the Rocky Mountains: Evidence for
652 long-range transport from Asia, boundary layer contributions, and plant mercury uptake.
653 *Atmospheric Environment*, 42(33), 7579–7589.

O'Dowd, C. D., Jimenez, J. L., Bahreini, R., Flagan, R. C., Seinfeld, J. H., Hämeri, K., Pirjola, L., Kulmala, M., Jennings, S. G., & Hoffmann, T. (2002). Marine aerosol formation from biogenic iodine emissions. *Nature*, 417(6889), 632–636. https://doi.org/10.1038/nature00775

Ordóñez, C., Lamarque, J.-F., Tilmes, S., Kinnison, D. E., Atlas, E. L., Blake, D. R., Sousa Santos, G., Brasseur, G., & Saiz-Lopez, A. (2012). Bromine and iodine chemistry in a global chemistry-climate model: description and evaluation of very short-lived oceanic sources. *Atmospheric Chemistry and Physics*, 12(3), 1423–1447. https://doi.org/10.5194/acp-12-1423-2012

Ortega, I., Berg, L. K., Ferrare, R. A., Hair, J. W., Hostetler, C. A., & Volkamer, R. (2016). Elevated aerosol layers modify the O_2–O_2 absorption measured by ground-based MAX-DOAS. *Journal of Quantitative Spectroscopy and Radiative Transfer*, 176, 34–49. https://doi.org/10.1016/j.jqsrt.2016.02.021

Platt, U. & Stutz, J. (2008). Differential Optical Absorption Spectroscopy: Principles and Applications. Berlin, Germany: Springer. https://doi.org/10.1007/978-3-540-75776-4

Prados-Roman, C., Cuevas, C. A., Hay, T., Fernandez, R. P., Mahajan, A. S., Royer, S.-J., Galí, M., Simó, R., Dachs, J., Großmann, K., Kinnison, D. E., Lamarque, J.-F., & Saiz-Lopez, A. (2015). Iodine oxide in the global marine boundary layer. *Atmospheric Chemistry and Physics*, 15(2), 583–593. https://doi.org/10.5194/acp-15-583-2015

Puentedura, O., Gil, M., Saiz-Lopez, A., Hay, T., Navarro-Comas, M., Gómez-Pelaez, A., Cuevas, E., Iglesias, J., & Gomez, L. (2012). Iodine monoxide in the north subtropical free troposphere. *Atmospheric Chemistry and Physics*, 12(11), 4909–4921. https://doi.org/10.5194/acp-12-4909-2012

Read, K. A., Mahajan, A. S., Carpenter, L. J., Evans, M. J., Faria, B. V. E., Heard, D. E., Hopkins, J. R., Lee, J. D., Moller, S. J., Lewis, A. C., Mendes, L., McQuaid, J. B., Oetjen, H., Saiz-Lopez, A., Pilling, M. J., & Plane, J. M. C. (2008). Extensive halogen-mediated ozone destruction over the tropical Atlantic Ocean. *Nature*, 453(7199), 1232–1235. https://doi.org/10.1038/nature07035

Rodgers, C.D. (2000). Inverse Methods for Atmospheric Sounding: Theory and Practice. Singapore: World Scientific Publishing. https://doi.org/10.1142/3171

Saiz-Lopez, A., Fernandez, R. P., Ordóñez, C., Kinnison, D. E., Gómez Martín, J. C., Lamarque, J.-F., & Tilmes, S. (2014). Iodine chemistry in the troposphere and its effect on ozone. *Atmospheric Chemistry and Physics*, 14(23), 13119–13143. https://doi.org/10.5194/acp-14-13119-2014

Saiz-Lopez, A., Lamarque, J.-F., Kinnison, D. E., Tilmes, S., Ordóñez, C., Orlando, J. J., Conley, A. J., Plane, J. M. C., Mahajan, A. S., Sousa Santos, G., Atlas, E. L., Blake, D. R., Sander, S. P., Schauffler, S., Thompson, A. M., & Brasseur, G. (2012). Estimating the climate significance of halogen-driven ozone loss in the tropical marine troposphere. *Atmospheric Chemistry and Physics*, 12(9), 3939–3949. https://doi.org/10.5194/acp-12-3939-2012

Saiz-Lopez, A., Sitkiewicz, S. P., Roca-Sanjuán, D., Oliva-Enrich, J. M., Dávalos, J. Z., Notario, R., Jiskra, M., Xu, Y., Wang, F., Thackray, C. P., Sunderland, E. M., Jacob, D. J., Travnikov, O., Cuevas, C. A., Acuña, A. U., Rivero, D., Plane, J. M. C., Kinnison, D. E., & Sonke, J. E. (2018). Photoreduction of gaseous oxidized mercury changes global atmospheric mercury speciation, transport and deposition. *Nature Communications*, 9(1), 4796. https://doi.org/10.1038/s41467-018-07075-3

Saiz-Lopez, A., Travnikov, O., Sonke, J. E., Thackray, C. P., Jacob, D. J., Carmona-García, J., Francés-Monerris, A., Roca-Sanjuán, D., Acuña, A. U., Dávalos, J. Z., Cuevas, C. A., Jiskra, M., Wang, F., Bieser, J., Plane, J. M. C., & Francisco, J. S. (2020). Photochemistry of oxidized Hg(I) and Hg(II) species suggests missing mercury oxidation in the troposphere. *Proceedings of the National Academy of Sciences*, 117(49), 30949–30956. https://doi.org/10.1073/pnas.1922486117

Schönhardt, A., Begoin, M., Richter, A., Wittrock, F., Kaleschke, L., Gómez Martín, J. C., & Burrows, J. P. (2012). Simultaneous satellite observations of IO and BrO over Antarctica. *Atmospheric Chemistry and Physics*, 12(14), 6565–6580. https://doi.org/10.5194/acp-12-6565-2012

Schönhardt, A., Richter, A., Theys, N., & Burrows, J. P. (2017). Space-based observation of volcanic iodine monoxide. *Atmospheric Chemistry and Physics*, 17(7), 4857–4870. https://doi.org/10.5194/acp-17-4857-2017

Schönhardt, A., Richter, A., Wittrock, F., Kirk, H., Oetjen, H., Roscoe, H. K., & Burrows, J. P. (2008). Observations of iodine monoxide columns from satellite. *Atmospheric Chemistry and Physics*, 8(3), 637–653. https://doi.org/10.5194/acp-8-637-2008

Shah, V., Jacob, D. J., Dang, R., Lamsal, L. N., Strode, S. A., Steenrod, S. D., Boersma, K. F., Eastham, S. D., Fritz, T. M., Thompson, C., Peischl, J., Bourgeois, I., Pollack, I. B., Nault, B. A., Cohen, R. C., Campuzano-Jost, P., Jimenez, J. L., Andersen, S. T., Carpenter, L. J., Sherwen, T. J., & Evans, M. J. (2023). Nitrogen oxides in the free troposphere: implications for tropospheric oxidants and the interpretation of satellite NO_2 measurements. *Atmospheric Chemistry and Physics*, 23(2), 1227–1257. https://doi.org/10.5194/acp-23-1227-2023

723 Shah, V., Jacob, D. J., Thackray, C. P., Wang, X., Sunderland, E. M., Dibble, T. S., Saiz-Lopez,
724 A., Černušák, I., Kellö, V., Castro, P. J., Wu, R., & Wang, C. (2021). Improved
725 Mechanistic Model of the Atmospheric Redox Chemistry of Mercury. *Environmental*
726 *Science & Technology*, 55(21), 14445–14456. https://doi.org/10.1021/acs.est.1c03160
727 Shepler, B. C., Balabanov, N. B., & Peterson, K. A. (2005). Ab Initio Thermochemistry
728 Involving Heavy Atoms: An Investigation of the Reactions Hg + IX (X = I, Br, Cl, O).
729 *The Journal of Physical Chemistry A*, 109(45), 10363–10372.
730 https://doi.org/10.1021/jp0541617
731 Sherwen, T., Evans, M. J., Carpenter, L. J., Andrews, S. J., Lidster, R. T., Dix, B., Koenig, T. K.,
732 Sinreich, R., Ortega, I., Volkamer, R., Saiz-Lopez, A., Prados-Roman, C., Mahajan, A.
733 S., & Ordóñez, C. (2016a). Iodine's impact on tropospheric oxidants: a global model
734 study in GEOS-Chem. *Atmospheric Chemistry and Physics*, 16(2), 1161–1186.
735 https://doi.org/10.5194/acp-16-1161-2016
736 Sherwen, T., Evans, M. J., Carpenter, L. J., Schmidt, J. A., & Mickley, L. J. (2017). Halogen
737 chemistry reduces tropospheric O_3 radiative forcing. *Atmospheric Chemistry and Physics*,
738 17(2), 1557–1569. https://doi.org/10.5194/acp-17-1557-2017
739 Sherwen, T., Schmidt, J. A., Evans, M. J., Carpenter, L. J., Großmann, K., Eastham, S. D., Jacob,
740 D. J., Dix, B., Koenig, T. K., Sinreich, R., Ortega, I., Volkamer, R., Saiz-Lopez, A.,
741 Prados-Roman, C., Mahajan, A. S., & Ordóñez, C. (2016b). Global impacts of
742 tropospheric halogens (Cl, Br, I) on oxidants and composition in GEOS-Chem.
743 *Atmospheric Chemistry and Physics*, 16(18), 12239–12271. https://doi.org/10.5194/acp-
744 16-12239-2016

Sipilä, M., Sarnela, N., Jokinen, T., Henschel, H., Junninen, H., Kontkanen, J., Richters, S., Kangasluoma, J., Franchin, A., Peräkylä, O., Rissanen, M. P., Ehn, M., Vehkamäki, H., Kurten, T., Berndt, T., Petäjä, T., Worsnop, D., Ceburnis, D., Kerminen, V.-M., Kulmala, M., & O'Dowd, C. (2016). Molecular-scale evidence of aerosol particle formation via sequential addition of HIO_3. *Nature*, 537(7621), 532–534. https://doi.org/10.1038/nature19314

Sive, B. C., Varner, R. K., Mao, H., Blake, D. R., Wingenter, O. W., & Talbot, R. (2007). A large terrestrial source of methyl iodide. *Geophysical Research Letters*, 34(17). https://doi.org/10.1029/2007GL030528

Spietz, P., Gómez Martín, J. C., & Burrows, J. P. (2005). Spectroscopic studies of the I_2/O_3 photochemistry. *Journal of Photochemistry and Photobiology A: Chemistry*, 176(1–3), 50–67. https://doi.org/10.1016/j.jphotochem.2005.08.023

Spinei, E., Cede, A., Herman, J., Mount, G. H., Eloranta, E., Morley, B., Baidar, S., Dix, B., Ortega, I., Koenig, T., & Volkamer, R. (2015). Ground-based direct-sun DOAS and airborne MAX-DOAS measurements of the collision-induced oxygen complex, O_2O_2, absorption with significant pressure and temperature differences. *Atmospheric Measurement Techniques*, 8(2), 793–809. https://doi.org/10.5194/amt-8-793-2015

Takashima, H., Kanaya, Y., Kato, S., Friedrich, M. M., van Roozendael, M., Taketani, F., Miyakawa, T., Komazaki, Y., Cuevas, C. A., Saiz-Lopez, A., & Sekiya, T. (2022). Full latitudinal marine atmospheric measurements of iodine monoxide. *Atmospheric Chemistry and Physics*, 22(6), 4005–4018. https://doi.org/10.5194/acp-22-4005-2022

Tirpitz, J.-L., Frieß, U., Hendrick, F., Alberti, C., Allaart, M., Apituley, A., Bais, A., Beirle, S., Berkhout, S., Bognar, K., Bösch, T., Bruchkouski, I., Cede, A., Chan, K. L., den Hoed,

M., Donner, S., Drosoglou, T., Fayt, C., Friedrich, M. M., Frumau, A., Gast, L., Gielen, C., Gomez-Martín, L., Hao, N., Hensen, A., Henzing, B., Hermans, C., Jin, J., Kreher, K., Kuhn, J., Lampel, J., Li, A., Liu, C., Liu, H., Ma, J., Merlaud, A., Peters, E., Pinardi, G., Piters, A., Platt, U., Puentedura, O., Richter, A., Schmitt, S., Spinei, E., Stein Zweers, D., Strong, K., Swart, D., Tack, F., Tiefengraber, M., van der Hoff, R., van Roozendael, M., Vlemmix, T., Vonk, J., Wagner, T., Wang, Y., Wang, Z., Wenig, M., Wiegner, M., Wittrock, F., Xie, P., Xing, C., Xu, J., Yela, M., Zhang, C., & Zhao, X. (2021). Intercomparison of MAX-DOAS vertical profile retrieval algorithms: studies on field data from the CINDI-2 campaign. *Atmospheric Measurement Techniques*, 14(1), 1–35. https://doi.org/10.5194/amt-14-1-2021

Van Roozendael, M., & the DOAS UV-VIS team at BIRA-IASB (2017). QDOAS: January 21, 2021 Release (version 3.4.5) [Software]. Royal Belgian Institute for Space Aeronomy. https://uv-vis.aeronomie.be/software/QDOAS/index.php (retrieved April 22, 2021)

Volkamer, R., Baidar, S., Campos, T. L., Coburn, S., DiGangi, J. P., Dix, B., Eloranta, E. W., Koenig, T. K., Morley, B., Ortega, I., Pierce, B. R., Reeves, M., Sinreich, R., Wang, S., Zondlo, M. A., & Romashkin, P. A. (2015). Aircraft measurements of BrO, IO, glyoxal, NO_2, H_2O, O_2–O_2 and aerosol extinction profiles in the tropics: comparison with aircraft-/ship-based in situ and lidar measurements. *Atmospheric Measurement Techniques*, 8(5), 2121–2148. https://doi.org/10.5194/amt-8-2121-2015

Wagner, T., Apituley, A., Beirle, S., Dörner, S., Friess, U., Remmers, J., & Shaiganfar, R. (2014). Cloud detection and classification based on MAX-DOAS observations. *Atmospheric Measurement Techniques*, 7(5), 1289–1320. https://doi.org/10.5194/amt-7-1289-2014

Wagner, T., Beirle, S., Benavent, N., Bösch, T., Chan, K. L., Donner, S., Dörner, S., Fayt, C., Frieß, U., García-Nieto, D., Gielen, C., González-Bartolome, D., Gomez, L., Hendrick, F., Henzing, B., Jin, J. L., Lampel, J., Ma, J., Mies, K., Navarro, M., Peters, E., Pinardi, G., Puentedura, O., Pukīte, J., Remmers, J., Richter, A., Saiz-Lopez, A., Shaiganfar, R., Sihler, H., Van Roozendael, M., Wang, Y., & Yela, M. (2019). Is a scaling factor required to obtain closure between measured and modelled atmospheric O_4 absorptions? An assessment of uncertainties of measurements and radiative transfer simulations for 2 selected days during the MAD-CAT campaign. *Atmospheric Measurement Techniques*, 12(5), 2745–2817. https://doi.org/10.5194/amt-12-2745-2019

Wang, X., Jacob, D. J., Downs, W., Zhai, S., Zhu, L., Shah, V., Holmes, C. D., Sherwen, T., Alexander, B., Evans, M. J., Eastham, S. D., Neuman, J. A., Veres, P. R., Koenig, T. K., Volkamer, R., Huey, L. G., Bannan, T. J., Percival, C. J., Lee, B. H., & Thornton, J. A. (2021). Global tropospheric halogen (Cl, Br, I) chemistry and its impact on oxidants. *Atmospheric Chemistry and Physics*, 21(18), 13973–13996. https://doi.org/10.5194/acp-21-13973-2021

Wang, S., Schmidt, J. A., Baidar, S., Coburn, S., Dix, B., Koenig, T. K., Apel, E., Bowdalo, D., Campos, T. L., Eloranta, E., Evans, M. J., DiGangi, J. P., Zondlo, M. A., Gao, R.-S., Haggerty, J. A., Hall, S. R., Hornbrook, R. S., Jacob, D., Morley, B., Pierce, B., Reevesj, M., Romashkin, P., ter Schure, A., Volkamer, R. (2015). Active and widespread halogen chemistry in the tropical and subtropical free troposphere. *Proceedings of the National Academy of Sciences*, 112(30), 9281–9286. https://doi.org/10.1073/pnas.1505142112

Wennberg, P. O., Brault, J. W., Hanisco, T. F., Salawitch, R. J., & Mount, G. H. (1997). The atmospheric column abundance of IO: Implications for stratospheric ozone. *Journal of*

Geophysical Research: Atmospheres, 102(D7), 8887–8898. https://doi.org/10.1029/96JD03712

Whalley, L. K., Furneaux, K. L., Gravestock, T., Atkinson, H. M., Bale, C. S. E., Ingham, T., Bloss, W. J., & Heard, D. E. (2007). Detection of iodine monoxide radicals in the marine boundary layer using laser induced fluorescence spectroscopy. *Journal of Atmospheric Chemistry*, 58(1), 19–39. https://doi.org/10.1007/s10874-007-9075-9

Williams, J., Gros, V., Atlas, E., Maciejczyk, K., Batsaikhan, A., Schöler, H. F., Forster, C., Quack, B., Yassaa, N., Sander, R., & van Dingenen, R. (2007). Possible evidence for a connection between methyl iodide emissions and Saharan dust. *Journal of Geophysical Research: Atmospheres*, 112(D7). https://doi.org/10.1029/2005JD006702

Wittrock, F., Müller, R., Richter, A., Bovensmann, H., & Burrows, J. P. (2000). Measurements of iodine monoxide (IO) above Spitsbergen. *Geophysical Research Letters*, 27(10), 1471–1474. https://doi.org/10.1029/1999GL011146

Wolfe, G. M., Marvin, M. R., Roberts, S. J., Travis, K. R., & Liao, J. (2016). The Framework for 0-D Atmospheric Modeling (F0AM) v3.1. *Geoscientific Model Development*, 9(9), 3309–3319. https://doi.org/10.5194/gmd-9-3309-2016

Zhao, X., Hou, X., & Zhou, W. (2019). Atmospheric Iodine (^{127}I and ^{129}I) Record in Spruce Tree Rings in the Northeast Qinghai-Tibet Plateau. *Environmental Science & Technology*, 53(15), 8706–8714. https://doi.org/10.1021/acs.est.9b01160

References From the Supporting Information

Chance, K., & Kurucz, R. L. (2010). An improved high-resolution solar reference spectrum for earth's atmosphere measurements in the ultraviolet, visible, and near infrared. *Journal of*

Quantitative Spectroscopy and Radiative Transfer, 111(9), 1289–1295. https://doi.org/10.1016/j.jqsrt.2010.01.036

Dowell, D. C., Alexander, C. R., James, E. P., Weygandt, S. S., Benjamin, S. G., Manikin, G. S., Blake, B. T., Brown, J. M., Olson, J. B., Hu, M., Smirnova, T. G., Ladwig, T., Kenyon, J. S., Ahmadov, R., Turner, D. D., Duda, J. D., & Alcott, T. I. (2022). The High-Resolution Rapid Refresh (HRRR): An Hourly Updating Convection-Allowing Forecast Model. Part I: Motivation and System Description. *Weather and Forecasting*, 37(8), 1371–1395. https://doi.org/10.1175/WAF-D-21-0151.1

Fleischmann, O. C., Hartmann, M., Burrows, J. P., & Orphal, J. (2004). New ultraviolet absorption cross-sections of BrO at atmospheric temperatures measured by time-windowing Fourier transform spectroscopy. *Journal of Photochemistry and Photobiology A: Chemistry*, 168(1–2), 117–132. https://doi.org/10.1016/j.jphotochem.2004.03.026

Giglio, L., Randerson, J. T., & van der Werf, G. R. (2013). Analysis of daily, monthly, and annual burned area using the fourth-generation global fire emissions database (GFED4). *Journal of Geophysical Research: Biogeosciences*, 118(1), 317–328. https://doi.org/10.1002/jgrg.20042

Guenther, A. B., Jiang, X., Heald, C. L., Sakulyanontvittaya, T., Duhl, T., Emmons, L. K., & Wang, X. (2012). The Model of Emissions of Gases and Aerosols from Nature version 2.1 (MEGAN2.1): an extended and updated framework for modeling biogenic emissions. *Geoscientific Model Development*, 5(6), 1471–1492. https://doi.org/10.5194/gmd-5-1471-2012

Hoesly, R. M., Smith, S. J., Feng, L., Klimont, Z., Janssens-Maenhout, G., Pitkanen, T., Seibert, J. J., Vu, L., Andres, R. J., Bolt, R. M., Bond, T. C., Dawidowski, L., Kholod, N.,

Kurokawa, J., Li, M., Liu, L., Lu, Z., Moura, M. C. P., O'Rourke, P. R., & Zhang, Q. (2018). Historical (1750–2014) anthropogenic emissions of reactive gases and aerosols from the Community Emissions Data System (CEDS). *Geoscientific Model Development*, 11(1), 369–408. https://doi.org/10.5194/gmd-11-369-2018

Finkenzeller, H., & Volkamer, R. (2022). O2–O2 CIA in the gas phase: Cross-section of weak bands, and continuum absorption between 297–500 nm. Journal of Quantitative Spectroscopy and Radiative Transfer, 279, 108063. https://doi.org/10.1016/j.jqsrt.2021.108063Lampel, J., Frieß, U., & Platt, U. (2015). The impact of vibrational Raman scattering of air on DOAS measurements of atmospheric trace gases. *Atmospheric Measurement Techniques*, 8(9), 3767–3787. https://doi.org/10.5194/amt-8-3767-2015

Meller, R., & Moortgat, G. K. (2000). Temperature dependence of the absorption cross sections of formaldehyde between 223 and 323 K in the wavelength range 225–375 nm. *Journal of Geophysical Research: Atmospheres*, 105(D6), 7089–7101. https://doi.org/10.1029/1999JD901074

Pukīte, J., & Wagner, T. (2016). Quantification and parametrization of non-linearity effects by higher-order sensitivity terms in scattered light differential optical absorption spectroscopy. *Atmospheric Measurement Techniques*, 9(5), 2147–2177. https://doi.org/10.5194/amt-9-2147-2016

Rothman, L. S., Gordon, I. E., Babikov, Y., Barbe, A., Chris Benner, D., Bernath, P. F., Birk, M., Bizzocchi, L., Boudon, V., Brown, L. R., Campargue, A., Chance, K., Cohen, E. A., Coudert, L. H., Devi, V. M., Drouin, B. J., Fayt, A., Flaud, J.-M., Gamache, R. R., Harrison, J. J., Hartmann, J.-M., Hill, C., Hodges, J. T., Jacquemart, D., Jolly, A.,

883 Lamouroux, J., Le Roy, R. J., Li, G., Long, D. A., Lyulin, O. M., Mackie, C. J., Massie,
884 S. T., Mikhailenko, S., Müller, H. S. P., Naumenko, O.V., Nikitin, A.V., Orphal, J.,
885 Perevalov, V., Perrin, A., Polovtseva, E. R., Richard, C., Smith, M. A. H., Starikova, E.,
886 Sung, K., Tashkun, S., Tennyson, J., Toon, G.C., Tyuterev, Vl. G., &Wagner, G. (2013).
887 The HITRAN2012 molecular spectroscopic database. *Journal of Quantitative*
888 *Spectroscopy and Radiative Transfer*, 130, 4–50.
889 https://doi.org/10.1016/j.jqsrt.2013.07.002
890 Rothman, L. S., Gordon, I. E., Barber, R. J., Dothe, H., Gamache, R. R., Goldman, A.,
891 Perevalov, V. I., Tashkun, S. A., & Tennyson, J. (2010). HITEMP, the high-temperature
892 molecular spectroscopic database. *Journal of Quantitative Spectroscopy and Radiative*
893 *Transfer*, 111(15), 2139–2150. https://doi.org/10.1016/j.jqsrt.2010.05.001
894 Serdyuchenko, A., Gorshelev, V., Weber, M., Chehade, W., & Burrows, J. P. (2014). High
895 spectral resolution ozone absorption cross-sections – Part 2: Temperature dependence.
896 *Atmospheric Measurement Techniques*, 7(2), 625–636. https://doi.org/10.5194/amt-7-
897 625-2014
898 Thalman, R., & Volkamer, R. (2013). Temperature dependent absorption cross-sections of O_2–
899 O_2 collision pairs between 340 and 630 nm and at atmospherically relevant pressure.
900 *Physical Chemistry Chemical Physics*, 15(37), 15371.
901 https://doi.org/10.1039/c3cp50968k
902 Vandaele, A. C., Hermans, C., Simon, P. C., Carleer, M., Colin, R., Fally, S., Mérienne, M. F.,
903 Jenouvrier, A., & Coquart, B. (1998). Measurements of the NO_2 absorption cross-section
904 from 42 000 cm−1 to 10 000 cm−1 (238–1000 nm) at 220 K and 294 K. *Journal of*

Quantitative Spectroscopy and Radiative Transfer, 59(3–5), 171–184.
https://doi.org/10.1016/S0022-4073(97)00168-4